

Between two descriptions of dark matter around a black hole: photon sphere, shadow, and lensing

M. F. Fauzi^{✉,†}, H. S. Ramadhan^{✉,†} and A. Sulaksono^{✉,‡}
Departemen Fisika, FMIPA, Universitas Indonesia, Depok 16424, Indonesia

We examine observational discrepancies of two widely used models describing anisotropic (dark) matter distributions around a black hole, focusing on their photon spheres, shadow radii, and lensing observables. The models considered are the vacuum and Einstein cluster dark matter model, characterized by negative and zero radial pressure, respectively. The analysis reveals that these models display contrasting photon sphere behavior. In particular, the Einstein cluster results in a more pronounced deviation in the shadow radius relative to the standard Schwarzschild black hole. Additionally, a distinctive lensing phenomenon associated with the matter halo is identified in both models.

I. INTRODUCTION

Black holes (BHs) at galactic centers are expected to be surrounded by dark matter (DM) distributions [1, 2]. A wide range of astrophysical observations provides strong evidence for the presence of DM in galaxies (see, e.g., [3, 4]). Motivated by this, numerous theoretical studies have explored the influence of DM-surrounded BHs, including the observational signatures from such systems [5–23]. These studies typically use phenomenological approaches to model DM distributions, some of which are constructed based on N-body simulations of galaxies [24].

However, there is still no consensus on how DM modifies the spacetime geometry in the vicinity of a BH. A number of studies adopt the simplifying assumption of a vacuum spacetime [12–18],

$$-g_{tt} = g_{rr}^{-1}, \quad (1)$$

effectively modeling the region around the BH as being oblivious to the presence of DM. It has been argued that this approximation captures the essential physical behavior of more general treatments [5]. In contrast, Cardoso *et al.* [6] used the *Einstein cluster* to model the (dark) matter distributions around a BH in a galaxy, which leads to a spacetime geometry that explicitly violates condition (1) due to the zero pressure matter distribution. This distinction raises the question: Does the simplified metric approximation adequately capture the observational signatures expected from a more complete Einstein cluster description of DM in the strong field regime?

This letter addresses the above question from the perspective of electromagnetic observations. While other studies focus on a single DM description, our work compares the two models and identifies their key distinguishing features. We consider two observational regimes. First, we examine the BH shadow as a probe of the

strong-field region. Although numerous studies have examined this context, most of them employ the assumption (1) [9–14]. This approach may provide insight into the characteristics of galactic DM inferred from the shadow of the central BH, particularly given observational results from the Event Horizon Telescope [25, 26]. Second, motivated by the fact that DM distributions typically span over galactic scales, we investigate a complementary observable in a weaker-field regime—namely, the image positions and time delays arising from gravitational lensing, following the formalism of Virbhadra [27]. This choice was motivated by the findings of Boehmer and Harko [28] who reported that the Newtonian approximation of the DM-induced deflection angle is about $\sim 77\%$ weaker than predictions from the Einstein cluster description of DM in the constant velocity region of galaxies. Kounatalis *et al.* [19] recently employed the Einstein cluster to investigate its impact on light deflection near the BH. In contrast, our work focuses on directly measurable lensing observables, as outlined above.

To proceed, we adopt the line element

$$ds^2 = \underbrace{-f e^\Phi dt^2}_{g_{tt}} + \underbrace{f^{-1} dr^2}_{g_{rr}} + r^2 d\Omega^2, \quad (2)$$

where $f \equiv f(r) = 1 - 2m(r)/r$. The function $m(r)$ is the mass function, while $\Phi \equiv \Phi(r)$ is the *shift function*. Throughout this work, we use geometrized units with $G = c = 1$.

II. (DARK) MATTER DESCRIPTION

When modeling the DM distribution as an anisotropic fluid with $T_\mu^\nu = \text{diag}(-\epsilon, p, p_t, p_t)$, there is no general consensus on the appropriate equation of state (EoS) for the radial pressure p . A number of studies adopt, for simplicity, the implicit choice $p = -\epsilon$, leading to the energy-momentum tensor

$$T_\mu^{\nu(V)} = \text{diag}(-\epsilon, -\epsilon, p_t, p_t). \quad (3)$$

We refer to this particular EoS as *vacuum* DM, since it is equivalent to a de Sitter-type EoS. This choice is, in

* Corresponding author.; muhammad.fahmi31@ui.ac.id

† hramad@sci.ui.ac.id

‡ anto.sulaksono@sci.ui.ac.id

fact, a consequence of the ansatz (1). It has been argued that this condition yields similar physical effects to more general cases where $-g_{tt} \neq g_{rr}^{-1}$ in the presence of DM [5]. Moreover, this ansatz provides a straightforward, widely used procedure for constructing rotating BH solutions via the Newman–Janis algorithm applied to the seed metric [15–17].

On the other hand, more recent studies employ a zero radial pressure, such that the energy–momentum tensor of the DM distribution becomes

$$T_\mu^{\nu(EC)} = \text{diag}(-\epsilon, 0, p_t, p_t). \quad (4)$$

This DM model is known as the *Einstein cluster* (EC), which describes a self-gravitating matter distribution composed of particles on stable circular orbits around the center [28], as originally proposed by Einstein [29]. The system is stabilized by the balance between gravity and the centrifugal forces from the orbiting matter, resulting in an anisotropic energy–momentum tensor with zero radial pressure. Unlike the vacuum DM case, a rotating solution for EC DM cannot be obtained via the Newman–Janis algorithm; its numerical rotating solution appeared only recently in Ref. [30]. Moreover, a recent study suggests that EC DM arises as a solution to a non-minimally coupled vector field interacting with gravity [31], indicating it may effectively behave as a vector field.

We conclude our brief comparison of the two DM models here. As shown in the following section, this seemingly minor difference gives rise to non-negligible modifications of the spacetime geometry in the near-BH region.

We now turn to the profile shape of the energy density $\epsilon(r)$, where most studies adopt effective distribution profiles. In this work, we employ the general form as in Ref. [8]

$$\epsilon(r) = \epsilon_0 \left(\frac{r}{a_0} \right)^{-\gamma} \left[1 + \left(\frac{r}{a_0} \right)^\sigma \right]^{\frac{\gamma-\beta}{\sigma}}, \quad (5)$$

where a_0 and ϵ_0 are constants that characterize the core size and the effective central “density,” respectively. The remaining parameters (σ, β, γ) determine the overall shape of the distribution and are model dependent. For instance, the Hernquist [32], Navarro–Frenk–White (NFW) [24], and Dehnen [33] profiles are obtained by assigning $(1, 4, 1)$, $(1, 3, 1)$, and $(1, 4, \gamma_D)$, respectively, where $\gamma_D \in [0, 3]$. One may directly notice that the Dehnen profile is a generalization of the Hernquist profile.

Earlier studies have reported the vanishing DM energy density near the BH horizon [1, 2]. Analytic approximations to this effect have been constructed by incorporating a cut-off factor into the energy density profile. For instance, the authors of Refs. [6–8] use

$$\epsilon(r) \rightarrow \epsilon(r) \left(1 - \frac{r_c}{r} \right), \quad (6)$$

where r_c denotes the cut-off radius at which the DM density vanishes. We refer to Eq. (6) as the *modified* energy

density profile. In Ref. [6], the authors assumed r_c to coincide with the BH horizon ($r_c = 2M_{BH}$). However, this assumption may lead to violations of the energy conditions and of the transverse speed of sound [34], motivating Ref. [7] to adopt a larger value of r_c —specifically $r_c = 4M_{BH}$, following the results of Ref. [2].

In the following discussion, we select two representative models to describe the DM energy density. We strictly employ the generalized modified form given in Eqs. (5) and (6). In particular, we choose the Hernquist profile and the Dehnen profile with $\gamma_D = 3/2$. Both profiles share the feature that the enclosed DM mass converges at large distances. This is in contrast to the NFW profile, where additional outer cut-off must be introduced to avoid a divergent total mass.

III. SPACETIME GEOMETRY

Having specified the matter distribution around the BH, the spacetime metric can be obtained by solving the Einstein field equations. The radial component is determined directly from the mass function $m(r)$, which represents the combined contribution of the BH and DM:

$$m(r) = M_{BH} + m_{DM}(r), \quad (7)$$

$$m_{DM}(r) = \int_{r_c}^r 4\pi\epsilon(\tilde{r}), d\tilde{r}. \quad (8)$$

The total Arnowitt–Deser–Misner (ADM) mass of the system is then $M_{ADM} = M_{BH} + M_{DM}$, where $M_{DM} = \lim_{r \rightarrow \infty} m_{DM}(r)$. The full analytic expressions of the mass functions corresponding to the modified Hernquist and Dehnen–3/2 profiles are provided in the [Supplementary Material](#).

Throughout our analysis, we consider two representative values for the DM total mass and core size: $M_{DM}/M_{BH} \in \{10, 100\}$ and $a_0/M_{BH} \in \{10^3, 10^4\}$. These choices are sufficient for our purposes, as they represent both diluted and relatively compact DM halos. We also adopt the same cut-off radius $r_c = 2M_{BH}$ as in Ref. [6].

Now we are left with the time component, in particular the shift function $\Phi(r)$. Following the formalism in Ref. [35], the shift function for each DM case satisfies

$$\frac{d\Phi^{(V)}}{dr} = 0, \quad \frac{d\Phi^{(EC)}}{dr} = \frac{8\pi\epsilon(r)r^2}{r - 2m(r)}. \quad (9)$$

In an asymptotically flat spacetime, one requires the boundary condition $\Phi(r)|_{r \rightarrow \infty} = 0$. This implies that EC DM introduces an additional redshift factor, since the shift function shall increase towards larger r . Meanwhile, vacuum DM simply leads to $-g_{tt} = g_{rr}^{-1}$. Additionally, Ref. [6] has obtained the analytic form of the $-g_{tt}$ component for the modified Hernquist profile with $r_c = 2M_{BH}$. Other approximate analytical solutions for generalized DM energy density profiles of Eq. (5) in the EC description have been obtained in Ref. [36].

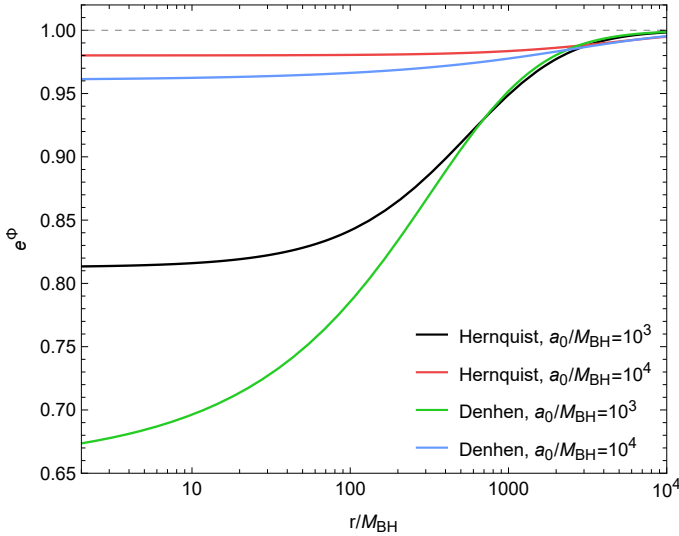


FIG. 1. The shift function for the EC DM with $M_{DM} = 100M_{BH}$. The gray dashed line represents the vacuum DM case, for which $\Phi(r) = 0$ everywhere.

We show the non-zero shift function for the EC DM in Fig. 1, where we set $M_{DM}/M_{BH} = 100$ for better visualization. The plot illustrates that the additional redshift factor extends beyond a_0 , and that a more compact configuration (smaller a_0) leads to a larger deviation from the zero shift function over a shorter radial range. Moreover, the Dehnen 3/2 profile produces a substantially stronger redshift factor near the BH horizon compared to the Hernquist profile, indicating that the discrepancy between EC DM and vacuum DM is likely model dependent. As we will show, this additional redshift factor plays a crucial role in electromagnetic observations, and its impact becomes non-negligible in the strong-field regime.

IV. RESULTING OBSERVABLES

Since we are dealing with a static and spherically symmetric spacetime, the geodesic equations for photons take a simple form. The two relevant equations are

$$\frac{d\phi}{dr} = \pm \frac{1}{r^2} \left[\frac{-g_{tt}g_{rr}}{b^{-2} - V(r)} \right]^{1/2}, \quad (10)$$

$$\frac{dt}{dr} = \pm \frac{1}{b} \left[\frac{g_{rr}(-g_{tt})^{-1}}{b^{-2} - V(r)} \right]^{1/2}, \quad (11)$$

where $V(r) \equiv -g_{tt}/r^2$ is the photon effective potential, $b \equiv L/E$ is the impact parameter, E and L denoting the photon's energy and angular momentum, respectively. The effective potential determines the turning point of photons approaching the system, and its form depends explicitly on $-g_{tt}$. Therefore, we expect EC DM to yield electromagnetic observables that differ from those obtained in the vacuum DM approximation.

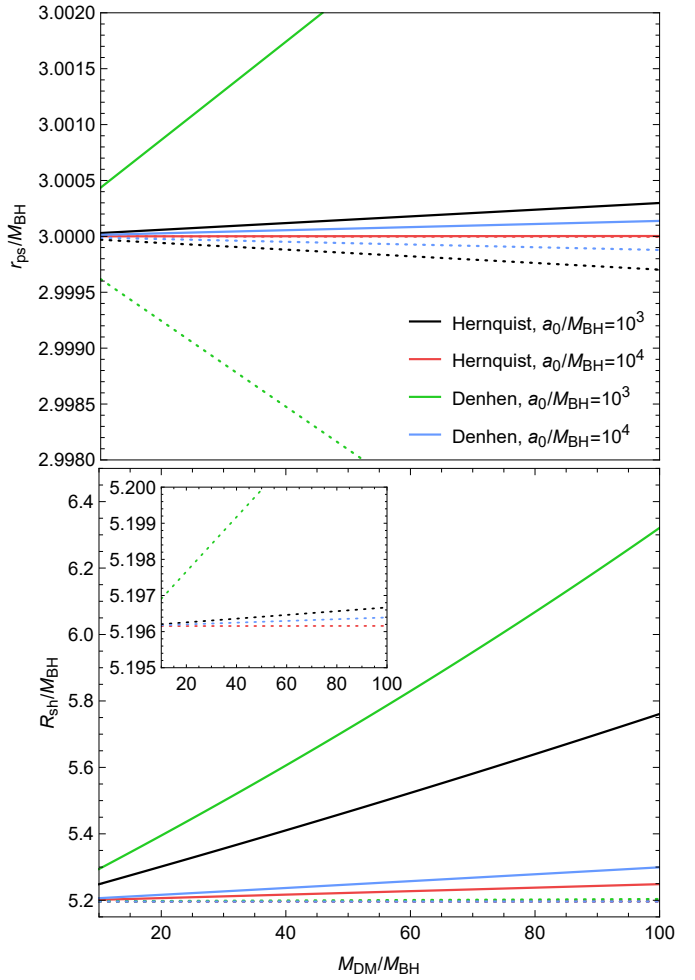


FIG. 2. (Top) Photon sphere radius and (Bottom) shadow radius for the EC DM and vacuum DM as functions of the DM mass, shown by solid and dotted lines, respectively.

Photon sphere and shadow—To calculate the BH shadow radius, one first needs to determine the location of the photon sphere r_{ps} . This is obtained by extremizing the effective potential, i.e., by solving $\partial_r V|_{r=r_{ps}} = 0$. Once the photon sphere is located, the critical impact parameter b_c follows from the relation $b_c = V(r_{ps})^{-1/2}$. Since the spacetime is asymptotically flat, the shadow radius R_{sh} , as well as its angular radius Θ_{sh} as seen by a distant observer at $D_{OL} \rightarrow \infty$, are given by [37]

$$R_{sh} \approx b_c, \quad \Theta_{sh} \approx \frac{R_{sh}}{D_{OL}}. \quad (12)$$

The resulting photon sphere radius, together with the BH shadow radius, is shown in Fig. 2. One can clearly observe that the photon sphere exhibits opposite trends in the two DM models: increasing the total DM mass shifts the photon sphere outward in the EC DM case, whereas in the vacuum DM case, it is shifted inward. The latter behavior commonly appears in models that adopt a de Sitter-like vacuum equation of state to describe the effec-

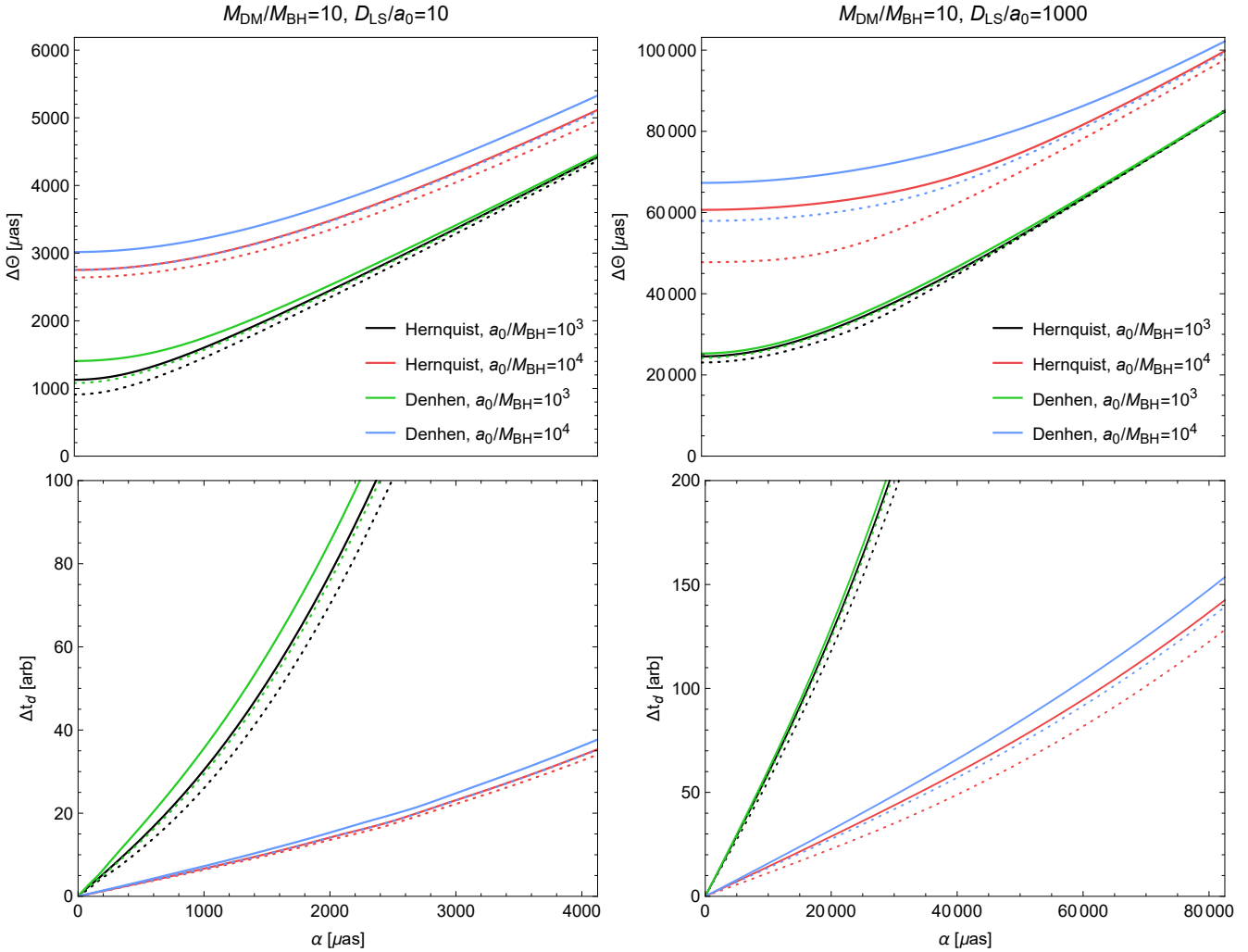


FIG. 3. (Top) Separation angle between the lensed primary and secondary images as a function of α , and (Bottom) their differential time delay, for EC DM (solid lines) and vacuum DM (dotted lines).

tive matter sourcing the geometry, as is typical in regular BH solutions (see, e.g., Refs. [38, 39]). Nonetheless, the deviation of the photon sphere from its Schwarzschild value ($r_{ps} = 3M_{BH}$) remains extremely small, even in the most compact configurations with small a_0 and large M_{DM} .

On the other hand, a significant discrepancy arises in the BH shadow radius. Specifically, in the EC DM model, increasing the DM mass results in a much steeper increase in the shadow radius than in the vacuum dark matter case. This behavior is directly linked to the additional redshift factor sourced by EC DM: it suppresses the g_{tt} , thereby lowering the peak of the photon effective potential and increasing the critical impact parameter. By contrast, in the vacuum DM model, the spacetime geometry near the BH remains nearly indistinguishable from the Schwarzschild solution, since the modification enters only through the mass function and becomes important predominantly at large distances.

This point is crucial when using BH shadow obser-

vations to constrain DM parameters. For example, by simply applying the M87* shadow radius constraint from Refs. [40, 41] to the Hernquist distribution with $a_0/M_{BH} = 10^3$, the EC DM model sets an upper bound on total DM mass at $M_{DM}/M_{BH} \approx 150$. In contrast, the vacuum DM model permits a much greater DM mass, up to the threshold where the halo forms a secondary horizon. This is consistent with Ref. [12] who found that notable changes in the BH shadow radius in vacuum DM models appear only when DM is highly concentrated near the BH, i.e., when $a_0 \sim \sqrt{3M_{BH}M_{DM}}$. Thus, the DM description—whether as an Einstein cluster or a vacuum fluid—must be carefully chosen, as it yields qualitatively different astrophysical conclusions.

Lensing observables—Next, we investigate the discrepancy between the two DM models in their lensing observables. Similar analyses of DM effects on lensing have recently been carried out in Ref. [19] for the EC DM model with the modified Hernquist profile of Ref. [6]. Numerous studies have also explored lensing

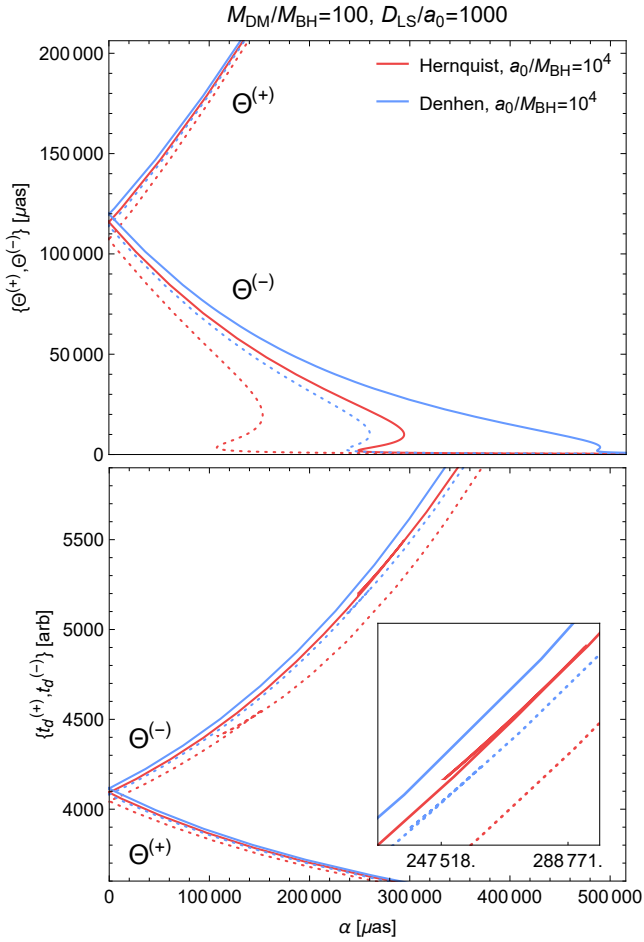


FIG. 4. (Top) Angular positions of the primary and secondary images as functions of α , and (Bottom) their corresponding time delays, for EC DM (solid lines) and vacuum DM (dotted lines), with $M_{DM}/M_{BH} = 100$ and $D_{LS}/a_0 = 1000$.

signatures in various vacuum DM scenarios (see, for example, Refs. [20–23] for some of the latest results).

The gravitational lensing setup is described as follows. A source located at an angular position α relative to the observer produces two observable images located at an angle $\Theta^{(+)}$ and $\Theta^{(-)}$, corresponding to the primary and secondary images, respectively [27]. For each image, the difference between the lapsed travel time in the curved spacetime and that in flat spacetime defines the time delay $t_d^{(\pm)}$. Since the primary (+) and secondary (−) rays follow different paths, they yield distinct time delays. The directly measurable quantities are the angular separation between the primary and secondary images, $\Delta\Theta = |\Theta^{(+)} - \Theta^{(-)}|$, and their differential time delay, $\Delta t_d = |t_d^{(+)} - t_d^{(-)}|$. An illustration and detailed description of the computation procedure of these observables are provided in the [Supplementary Material](#).

For our purposes, we assume the source lies *within* or *near* the DM halo at a distance D_{LS} from the BH, while

the observer is at D_{OL} from the BH and positioned in a region where spacetime is effectively flat ($g_{rr} \approx -g_{tt} \approx 1$). This setup ensures a significant influence of the redshift factor, particularly on the primary images. If both D_{OL} and D_{LS} were very large, light rays of the primary images would approach closest to the BH outside the DM halo, where spacetime resembles a Schwarzschild geometry and the DM-induced redshift factor is negligible. We specifically set $D_{OL}/M_{BH} \approx 10^{11}$, and choose the source distance from the lens as $D_{LS}/a_0 \in \{10, 1000\}$. Observable quantities are presented in arbitrary units to facilitate the comparison between the two DM descriptions. As a reference, using Eq. (12), the shadow angular radius Θ_{sh} for a Schwarzschild BH in this setup is $\sim 10.7, \mu\text{as}$, while the angular radius of the DM core with $a_0/M_{BH} = 10^3$ is $\sim 2.06 \times 10^3 \mu\text{as}$.

We compare the EC and vacuum DM predictions for both observables in Fig. 3, focusing on the case with $M_{DM}/M_{BH} = 10$. In all configurations, EC DM produces stronger lensing than vacuum DM for image separation and differential time delay. The largest differences on the image position appear when the source, lens, and BH are aligned ($\alpha = 0$), resulting in the so-called Einstein ring [42]. The size of this discrepancy depends on both the source distance D_{LS} and the DM core size. A smaller core causes more significant differences for sources near the BH, while a larger core amplifies the effect for more distant sources. EC DM predicts an Einstein ring diameter $\sim 4\% - 56\%$ larger than vacuum DM, depending on configuration and source distance.

In the setup with $M_{DM}/M_{BH} = 100$ and $D_{LS}/a_0 = 10^3$, in Fig. 4, we find an interesting phenomenon arising from the DM distribution: there exists a range of α that produces multiple secondary images across all DM models. This phenomenon was also reported in a recent lensing study of EC DM around a BH [19] on the deflection angle. A similar feature is clearly visible in Fig. 4c of Ref. [11], although they consider a different DM and lensing configuration. The discrepancy between the two DM descriptions is reflected in the positions and separations of the multiple secondary images. Vacuum DM produces multiple lensed images at smaller source inclinations from the observer, but with a larger separation than those of the EC DM. However, the time delays associated with these multiple lensed images are roughly the same, implying that all events in these lensed images occurred at the same time as observed by a distant observer. This may become an important potential signature of DM around a BH, regardless of the chosen description of the DM halo itself.

V. CONCLUSION AND DISCUSSION

We have compared two models of anisotropic dark matter (DM) distributions around a black hole (BH): the vacuum DM model and the Einstein cluster (EC) DM model. The primary physical distinction is the presence

of radial pressure, which influences the time component of the metric. Vacuum DM acts as a “de Sitter” fluid and does not alter the shift function on the metric, whereas EC DM introduces an additional redshift factor whose behavior depends on the energy density profile. Consequently, the two models produce distinct signatures in electromagnetic observables. Our analysis shows that the photon sphere radius increases with DM mass in the EC model, while it shifts slightly inward for vacuum DM. Notably, EC DM exerts a significantly stronger effect on the BH shadow radius compared to vacuum DM. Lensing observables, including image positions and the differential time delay between primary and secondary images, also exhibit substantial differences between the two models.

We therefore conclude that the theoretical modeling of the DM halo surrounding a BH is crucial for determining its electromagnetic observables. If the actual DM distribution is best represented by an Einstein cluster, the vacuum DM approximation is insufficient for probing the geometry near the BH. Combining shadow measurements with strong-field lensing signatures offers a promising approach to distinguish between different DM models, particularly when supplemented by independent data from the dynamics of nearby objects. Future observational

data may enable the exclusion or confirmation of competing DM descriptions.

Several caveats warrant attention. The adopted setup and assumptions may not fully capture a realistic cosmological settings. For example, time delay analyses in large scale gravitational lensing (e.g., HE 0435-1223 [43]) typically include cosmic expansion to infer the Hubble constant, which was not addressed in this study. Furthermore, lensing observables, especially time delays, are sensitive to perturbing matter both near the lens and along the line of sight. Future work that incorporates the cosmological constant into the Einstein field equations and accounts for perturbers would be valuable.

Nevertheless, our results capture robust features of strong-field lensing around BHs embedded in DM and remain relevant for future theoretical and observational investigations.

ACKNOWLEDGEMENTS

We thank Byon Jayawiguna, Faris Darmawan, and Naufal Athaullah for the valuable discussions on the early stage of this work. HSR is supported by Hibah PUTI Q1 UI No. PKS-196/UN2.RST/HKP.05.00/2025.

[1] P. Gondolo and J. Silk, *Phys. Rev. Lett.* **83**, 1719 (1999), [arXiv:astro-ph/9906391](https://arxiv.org/abs/astro-ph/9906391).

[2] L. Sadeghian, F. Ferrer and C. M. Will, *Phys. Rev. D* **88**, 063522 (2013), [arXiv:1305.2619](https://arxiv.org/abs/1305.2619).

[3] D. Clowe, M. Bradac, A. H. Gonzalez, M. Markevitch, S. W. Randall, C. Jones and D. Zaritsky, *Astrophys. J. Lett.* **648**, L109 (2006), [arXiv:astro-ph/0608407](https://arxiv.org/abs/astro-ph/0608407).

[4] G. Bertone and D. Hooper, *Rev. Mod. Phys.* **90**, 045002 (2018), [arXiv:1605.04909](https://arxiv.org/abs/1605.04909).

[5] Z. Xu, X. Hou, X. Gong and J. Wang, *JCAP* **09**, 038 (2018), [arXiv:1803.00767](https://arxiv.org/abs/1803.00767).

[6] V. Cardoso, K. Destounis, F. Duque, R. P. Macedo and A. Maselli, *Phys. Rev. D* **105**, L061501 (2022), [arXiv:2109.00005](https://arxiv.org/abs/2109.00005).

[7] N. Spenney, E. Berti, V. Cardoso and A. Maselli, *Phys. Rev. D* **109**, 084068 (2024), [arXiv:2401.00932](https://arxiv.org/abs/2401.00932).

[8] E. Figueiredo, A. Maselli and V. Cardoso, *Phys. Rev. D* **107**, 104033 (2023), [arXiv:2303.08183](https://arxiv.org/abs/2303.08183).

[9] Y. S. Myung, *Eur. Phys. J. C* **85**, 1116 (2025), [arXiv:2502.13397](https://arxiv.org/abs/2502.13397).

[10] S. J. Ma, T. C. Ma, J. B. Deng and X. R. Hu, *Mod. Phys. Lett. A* **38**, 2350104 (2023), [arXiv:2206.12820](https://arxiv.org/abs/2206.12820).

[11] S. V. M. C. B. Xavier, H. C. D. Lima, Junior. and L. C. B. Crispino, *Phys. Rev. D* **107**, 064040 (2023), [arXiv:2303.17666](https://arxiv.org/abs/2303.17666).

[12] R. A. Konoplya, *Phys. Lett. B* **795**, 1 (2019), [arXiv:1905.00064](https://arxiv.org/abs/1905.00064).

[13] X. Hou, Z. Xu, M. Zhou and J. Wang, *JCAP* **07**, 015 (2018), [arXiv:1804.08110](https://arxiv.org/abs/1804.08110).

[14] K. Jusufi, M. Jamil and T. Zhu, *Eur. Phys. J. C* **80**, 354 (2020), [arXiv:2005.05299](https://arxiv.org/abs/2005.05299).

[15] Q. X. Liu, Y. P. Hu, T. T. Sui and Y. S. An, *Phys. Dark Univ.* **46**, 101624 (2024), [arXiv:2406.04611](https://arxiv.org/abs/2406.04611).

[16] K. J. He, G. P. Li, C. Y. Yang and X. X. Zeng, *Eur. Phys. J. C* **85**, 662 (2025), [arXiv:2411.11680](https://arxiv.org/abs/2411.11680).

[17] Z. Xu, J. Wang and X. Hou, *Class. Quant. Grav.* **35**, 115003 (2018), [arXiv:1711.04538](https://arxiv.org/abs/1711.04538).

[18] D. Liu, Y. Yang, S. Wu, Y. Xing, Z. Xu and Z. W. Long, *Phys. Rev. D* **104**, 104042 (2021), [arXiv:2104.04332](https://arxiv.org/abs/2104.04332).

[19] G. Kounitalis, A. G. Suvorov and K. Destounis, [arXiv:2508.19333](https://arxiv.org/abs/2508.19333).

[20] R. C. Pantig and A. Övgün, *Eur. Phys. J. C* **82**, 391 (2022), [arXiv:2201.03365](https://arxiv.org/abs/2201.03365).

[21] Y. G. Liu, C. K. Qiao and J. Tao, *JCAP* **10**, 075 (2024), [arXiv:2312.15760](https://arxiv.org/abs/2312.15760).

[22] N. U. Molla, H. Chaudhary, S. Capozziello, F. Atamurotov, G. Mustafa and U. Debnath, *Phys. Dark Univ.* **47**, 101804 (2025), [arXiv:2501.09439](https://arxiv.org/abs/2501.09439).

[23] N. U. Molla, H. Chaudhary, G. Mustafa, F. Atamurotov, U. Debnath and D. Arora, *Eur. Phys. J. C* **84**, 574 (2024), [arXiv:2310.14234](https://arxiv.org/abs/2310.14234).

[24] J. F. Navarro, C. S. Frenk and S. D. M. White, *Astrophys. J.* **490**, 493 (1997), [arXiv:astro-ph/9611107](https://arxiv.org/abs/astro-ph/9611107).

[25] K. Akiyama *et al.* [Event Horizon Telescope], *Astrophys. J. Lett.* **875**, L1 (2019), [arXiv:1906.11238](https://arxiv.org/abs/1906.11238).

[26] K. Akiyama *et al.* [Event Horizon Telescope], *Astrophys. J. Lett.* **930**, L12 (2022) [arXiv:2311.08680](https://arxiv.org/abs/2311.08680).

[27] K. S. Virbhadra, *Phys. Rev. D* **79**, 083004 (2009), [arXiv:0810.2109](https://arxiv.org/abs/0810.2109).

[28] C. G. Boehmer and T. Harko, *Mon. Not. Roy. Astron. Soc.* **379**, 393-398 (2007), [arXiv:0705.1756](https://arxiv.org/abs/0705.1756).

[29] A. Einstein, *Annals Math* **40**, 922-936 (1939).

- [30] P. G. S. Fernandes and V. Cardoso, *Phys. Rev. Lett.* **135**, 211403 (2025), arXiv:2507.04389.
- [31] P. G. S. Fernandes and V. Cardoso, arXiv:2505.00563.
- [32] L. Hernquist, *Astrophys. J.* **356**, 359 (1990).
- [33] W. Dehnen, *Mon. Not. Roy. Astron. Soc.* **265**, 250 (1993).
- [34] S. Datta, *Phys. Rev. D* **109**, 104042 (2024), arXiv:2312.01277.
- [35] M. F. Fauzi, B. N. Jayawiguna, H. S. Ramadhan and A. Sulaksono, *Eur. Phys. J. C* **85**, 903 (2025), arXiv:2508.18072.
- [36] R. A. Konoplya and A. Zhidenko, *Astrophys. J.* **933**, 166 (2022), arXiv:2202.02205.
- [37] V. Perlick and O. Y. Tsupko, *Phys. Rept.* **947**, 1 (2022), arXiv:2105.07101.
- [38] S. Gera, S. Kumar, P. Dutta Roy and S. Chakrabarti, *JCAP* **07**, 065 (2025), arXiv:2411.11970.
- [39] R. Carballo-Rubio, F. Di Filippo, S. Liberati and M. Visser, *JHEP* **08**, 046 (2023), arXiv:2211.05817.
- [40] D. Psaltis *et al.* [Event Horizon Telescope], *Phys. Rev. Lett.* **125**, 141104 (2020), arXiv:2010.01055.
- [41] P. Kocherlakota *et al.* [Event Horizon Telescope], *Phys. Rev. D* **103**, 104047 (2021), arXiv:2105.09343.
- [42] J. Wambsganss, *Living Rev. Rel.* **1**, 12 (1998), arXiv:astro-ph/9812021.
- [43] K. C. Wong *et al.* [H0LiCOW], *Mon. Not. Roy. Astron. Soc.* **465**, 4895 (2017), arXiv:1607.01403.

SUPPLEMENTARY MATERIAL

The mass function of the dark matter distribution

For a perfect fluid description of the energy-momentum tensor in a static and spherically symmetric spacetime, the mass function (also known as the Misner-Sharp mass) can be calculated by solving the Einstein field equation. In our DM case, since there is no DM mass contribution inside the cut-off radius r_c , the integration of the mass function begins at r_c , as shown in Eq. (8). The resulting mass functions for the modified Hernquist and Denhen 3/2 energy density profiles used in this work can be computed analytically, yielding

$$m_{DM}^{(H)}(r) = M_{DM} \frac{(r - r_c)^2}{(a_0 + r_c)^2} \quad (\text{S.1})$$

$$m_{DM}^{(D)}(r) = M_{DM} \xi^{-1} \left[\frac{a_0 \sqrt{r} [a_0(r - 3r_c) - 2r_c r]}{(a_0 + r)^{3/2}} + \eta \right] \quad (\text{S.2})$$

$$\xi = a_0(a_0 - 2r_c) + \eta$$

$$\eta = 2r_c a_0 \sqrt{\frac{r_c}{a_0 + r_c}}$$

where the superscripts (H) and (D) denote the Hernquist and Denhen 3/2 mass profiles, respectively. The total DM mass M_{DM} , also referred to as the Arnowitt-Deser-Misner (ADM) mass, is defined by the condition $M_{DM} = \lim_{r \rightarrow \infty} m(r)$, which is satisfied for both modified Hernquist and Denhen 3/2 profiles above.

Computing the lensing observables

Solving the geodesic equation to compute the lensing observables fully numerically for our case requires several steps. An illustration of the corresponding lensing configuration is shown in Fig. S.1.

The lensing observables are described as follows. Two images—namely, the primary image $I^{(+)}$ at an angle $\Theta^{(+)}$ and the secondary image $I^{(-)}$ at an angle $\Theta^{(-)}$ —of a light source located at a distance D_{LS} from the BH and at an angle α with respect to the observer are observed on opposite sides of the BH. The light rays producing both images travel longer paths than they would in flat spacetime and, further affected by the redshift factor, require a longer time to reach the observer. This results in the time delays $t_d^{(\pm)}$ for the two images.

The quantities of interest for observation are then the angular image positions $\Theta^{(\pm)}$ and the time delays $t_d^{(\pm)}$ as functions of α . All of these quantities can be obtained by solving the null geodesic equations given in Eqs. (10) and (11).

The integration of the geodesic equation in Eq. (10) begins from the observer at D_{OL} to the closest approach distance r_0 —also known as the turning point, where $V(r_0) = b^{-2}$ —and is then continued to the source location at D_{LS} . The resulting quantity is ϕ_{end} , which is written as

$$\phi_{end} = \int_{D_{OL}}^{r_0} \left(\frac{d\phi}{dr} \right) dr + \int_{r_0}^{D_{LS}} \left(\frac{d\phi}{dr} \right) dr. \quad (\text{S.3})$$

Here, the impact parameter b is used as the input, such that $\phi_{end} \rightarrow \phi_{end}(b)$. From this quantity, one obtains the relation between the source angle α and ϕ_{end} ,

$$\sin \alpha = \frac{D_{LS}}{d} \sin \phi_{end}, \quad (\text{S.4})$$

where $d = \sqrt{D_{LS}^2 + D_{OL}^2 - 2D_{LS}D_{OL} \cos \phi_{end}}$, which gives $\alpha(b)$. Meanwhile, the image angle $\Theta^{(\pm)}$ is computed straightforwardly from elementary geometry,

$$\Theta^{(\pm)} = \tan^{-1} \frac{b}{D_{OL}}, \quad (\text{S.5})$$

yielding $\Theta^{(\pm)}(b)$.

In the simple case—*i.e.*, when there is no multiple value of b corresponding to a single α —the relation $\Theta^{(\pm)}(\alpha)$ can be obtained numerically via interpolation. The primary (+) or secondary (-) images are selected based on the sign

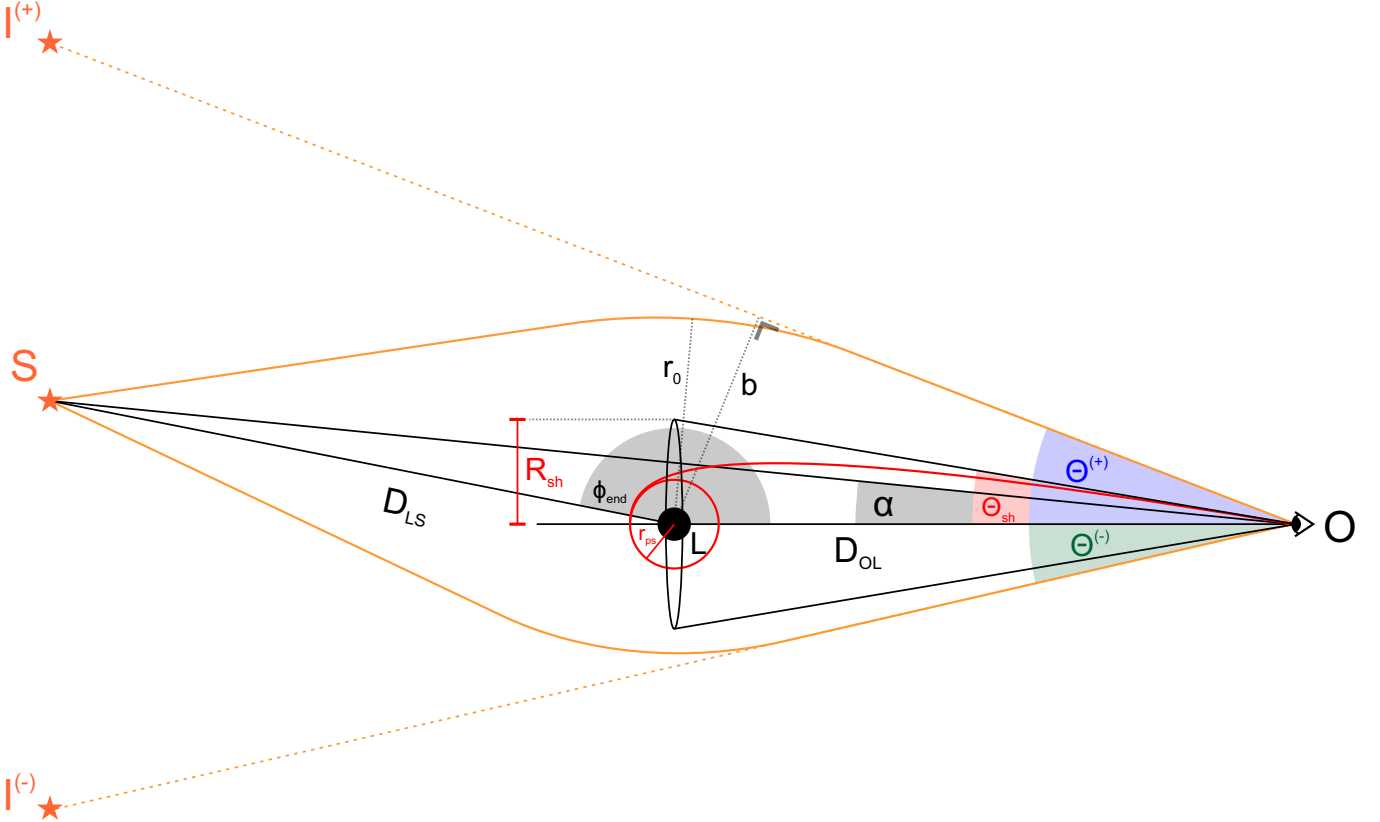


FIG. S.1. Illustration of the BH lensing setup.

of α : if $\alpha > 0$, the result is assigned to the primary image, whereas for $\alpha < 0$ it corresponds to the secondary image. Afterward, the magnitude of α for the secondary image can be taken as positive. This is permissible due to spherical symmetry, which allows a 180° rotation around the x -axis without changing the physical configuration.

However, the same interpolation procedure cannot be applied when there exist multiple values of b for a given α . This occurs in our configuration with $M_{DM}/M_{BH} = 100$ and $D_{LS}/a_0 = 10^3$. In this situation, we instead present the relation $\Theta^{(\pm)}(\alpha)$ using a parametric plot, as shown in Fig. 3, with the absolute value of α placed on the x -axis.

Additionally, the time delay t_d is computed in a similar manner. The integration of Eq. (11) gives the elapsed time required for a photon emitted from the source to reach the observer. It is expressed as

$$t_{end} = \left| \int_{D_{OL}}^{r_0} \left(\frac{dt}{dr} \right) dr \right| + \left| \int_{r_0}^{D_{LS}} \left(\frac{dt}{dr} \right) dr \right|, \quad (S.6)$$

where the absolute values are used to avoid negative contributions, since the elapsed time in both segments must be positive. This provides $t_{end}(b)$. Because the distance d depends on $\phi_{end}(b)$, we have $d \rightarrow d(b)$, and the time delay can be written as

$$t_d(b) = t_{end}(b) - d(b). \quad (S.7)$$

The same numerical procedure used to obtain $\Theta^{(\pm)}(\alpha)$ can then be applied to acquire $t_d(\alpha)$.